Journal of the European Ceramic Society 43 (2023) 6925–6933

Contents lists available at ScienceDirect

Journal of the European Ceramic Society

journal homepage: www.elsevier.com/locate/jeurceramsoc

# Reactive FAST/SPS sintering of strontium titanate as a tool for grain boundary engineering

M. Pascal Zahler [a], Dylan Jennings [a,b], Moritz Kindelmann [a,b,c], Olivier Guillon [a,d,e], Wolfgang Rheinheimer [a,d,*]

[a] Forschungszentrum Jülich GmbH, Institute of Energy and Climate Research, Materials Synthesis and Processing (IEK-1), 52425 Jülich, Germany
[b] Ernst-Ruska Centre for Microscopy and Spectroscopy with Electrons (ER-C), Forschungszentrum Jülich, 52425 Jülich, Germany
[c] RWTH Aachen University, Central Facility for Electron Microscopy (GFE), 52074 Aachen, Germany
[d] RWTH Aachen University, Institute of Mineral Engineering, RWTH Aachen University, 52064 Aachen, Germany
[e] Jülich Aachen Research Alliance: JARA-Energy, 52425 Jülich, Germany

ARTICLE INFO

*Keywords:*
Strontium titanate
Microstructure
Space charge
Electrochemical impedance spectroscopy
Spark Plasma Sintering

ABSTRACT

A high-pressure FAST/Spark Plasma Sintering method was used to produce dense $SrTiO_3$ ceramics at temperatures of 1050 °C, more than 250 °C below typical sintering temperatures. Combining SPS with solid-state reactive sintering further improves densification. The process resulted in fine-grained microstructures with grain sizes of ~300 nm. STEM-EDS was utilized for analyzing cationic segregation at grain boundaries, revealing no cationic segregation at the GBs after SPS. Electrochemical impedance spectroscopy indicates the presence of a space charge layer. Space charge thicknesses were calculated according to the plate capacitor equation and the Mott-Schottky model. They fit the expected size range, yet the corresponding space charge potentials are lower than typical values of conventionally processed $SrTiO_3$. The low space charge potential was associated to low cationic GB segregation after SPS and likely results in better grain boundary conductivity. The findings offer a path to tailor grain boundary segregation and conductivity in perovskite ceramics.

## 1. Introduction

Spark plasma sintering (SPS) is a field-assisted sintering technique (FAST) allowing the processing and densification of ceramic and metal powders at low temperatures in short times [1–3]. It is used in the manufacturing of refractory and ultra-high-temperature materials, advanced functional materials, transparent ceramics and nanocrystalline materials [2,4].

During SPS sintering, heating of specimens is provided by Joule heating of the pressing tool, which is realized by applying a pulsed DC voltage. Joule heating allows high heating rates [1,4,5], which facilitate rapid densification of powder compacts [6]. In combination with high cooling rates, materials with non-equilibrium compositions can be processed via SPS [2,4]. A mechanical pressure during sintering further enhances densification [7–9].

High pressure SPS can be utilized to achieve high densification at low temperatures. Normally, ceramics are sintered at high temperatures, where grain boundary and lattice diffusion are the dominating process, which enable densification without additional pressure [9,10]. At lower temperatures, surface diffusion dominates mass transport causing particle coarsening, which reduces the driving force for densification and can prevent complete consolidation [11,12]. Densification and sintering at lower temperatures are feasible by applying very high pressures during SPS. Surface diffusion in combination with high pressures were reported to enable densification by grain sliding during high pressure SPS [10]. Water vapor was reported to further enhance surface diffusion by introducing surface vacancies and hydroxyl ions at the sintering necks [13], which seems to be beneficial for grain sliding processes.

Another method to reduce the sintering temperature is solid-state reactive sintering [14,15]. During reactive sintering, the sintering process runs parallel to a chemical reaction. The product of the chemical reaction is the desired phase that normally is synthesized before sintering. During solid state reactive sintering, the driving force of sintering is increased by reduction in chemical potential [15] and kinetics of mass transport are significantly enhanced [16] by the chemical reaction. In the last decade, different proton-conducting perovskites were

* Corresponding author at: Forschungszentrum Jülich GmbH, Institute of Energy and Climate Research, Materials Synthesis and Processing (IEK-1), 52425 Jülich, Germany.
*E-mail address:* w.rheinheimer@fz-juelich.de (W. Rheinheimer).

https://doi.org/10.1016/j.jeurceramsoc.2023.07.021
Received 29 June 2023; Accepted 11 July 2023
Available online 17 July 2023

successfully sintered via a solid-state reactive sintering process (SSRS) [17–19].

In recent years, hydrothermal sintering ('cold-sintering') has gained attention because of its potential to achieve densification at temperatures below 400 °C [20–22]. Cold-sintering enables densification of powder compacts using a sintering aid like water while applying high pressures [23–25]. Yet for multicomponent materials, such as perovskites, this process has to be combined with an hydrothermal synthesis and a post-sintering annealing step to achieve high consolidation and phase purity [20–22,24].

Strontium titanate ($SrTiO_3$) is a well-studied material, and many sintering methods have been tested for its densification: conventional sintering [26], cold-sintering [22,23], FAST/SPS [6], UHS [27], flash sintering [28–31], blacklight sintering [32] and hot pressing (HP) [33,34]. Additionally, the sintering and grain growth kinetics of $SrTiO_3$ are well understood [35–38].

For any sintering process, understanding grain boundary physics is important. In $SrTiO_3$ and other perovskite ceramics, space charge layers form due to the segregation of oxygen vacancies to the grain boundary core [39–44]. The resulting positive charge leads other point defects (dopants, cationic vacancies, electrons & electron holes) to either segregate or deplete near the grain boundary depending on their charge [39,40,44]. Space charge layers are detrimental for electronic properties as they often increase the grain boundary resistance and thereby decrease the overall [45–49]. The formation of space charge layers in thermodynamic equilibrium is possible only for long periods of time or at high temperatures which is the case for conventional sintering methods [44,48,50,51]. High-pressure SPS on the other hand offers a unique opportunity for space charge engineering in ceramic materials as densification occurs at low temperatures in short time periods, where a full equilibration of the grain boundary including the space charge layer may not occur.

In this paper, high pressure SPS was performed to procure highly dense $SrTiO_3$ ceramics below typical temperatures needed to form equilibrium space charge layers. The SPS process was combined with SSRS process to aid in the densification process. The SPS samples were analyzed for their relative densities, grain sizes, cationic segregation at their GBs and their grain boundary impedance. The results were compared with data from conventionally sintered (CS) $SrTiO_3$ samples. The lower sintering temperature and time prevented the formation of equilibrium space charge layers at the grain boundaries. Due to the small grain size after SPS sintering, grain boundaries dominated even though the GB conductivity of the SPS samples was comparably higher than that of the conventionally sintered samples.

## 2. Experimental procedure

### 2.1. Powder synthesis

Stoichiometric $SrTiO_3$ powders were synthesized via the mixed oxide/carbonate method from $SrCO_3$ (Sigma Aldrich, ≥99.9%) and $TiO_2$ (rutile, Sigma Aldrich, USA, ≥99.9%). The powder was ball milled in isopropanol for 15 cycles of 5 min each at 400 rpm in a planetary ball mill (PM400, Retsch, Germany). $ZrO_2$ milling balls with a diameter of 3 mm were used for milling. Because of the high-energy ball milling, Zr impurities are introduced into the powders changing their stoichiometry to slightly B-site rich compositions. After milling the powder was sieved using a 150 μm sieve in a vibratory sieve shaker (Analysette 3 Spartan, Retsch, Germany). Three different calcination methods were used to investigate the impact of phase purity and reactivity during reactive SPS sintering. SPS samples were made from not-calcined precursor material mixtures (SPS-NC samples), partially calcined powders synthesized at 900 °C for 3 h (SPS-PC samples) and fully calcined powders synthesized at 975 °C for 3 h (SPS-FC samples). Fully calcined powder was also used for conventionally sintered samples (CS samples). Before sintering, the calcined powders were again milled for 6 cycles of 5 min each at 350 rpm in the same planetary ball mill (PM400) with 3 mm $ZrO_2$ milling balls in isopropanol. After milling the powders were sieved through 45 μm sieves.

### 2.2. Sintering experiments

For conventional sintering, green bodies were pre-pressed uniaxially and further densified by cold-isostatic pressing at 400 MPa. Conventional sintering was done in air at 1425 °C for 1 h. SPS samples were sintered using a spark plasma sintering furnace HP-D5 (FCT Systeme GmbH, Germany). 2 g of either powder batch was filled in a TZM (Mo based alloy, Plansee, Austria) pressing die lined with graphite foil. The TZM pressing die allows much higher pressures at temperatures used in this study compared to graphite dies. Then, 100 μl of distilled $H_2O$ was added to the powder with a pipette before the first densification step at 6 kN by uniaxial pressing. Water was added for partial dissolution of the powder's surface. Water vapor was also reported to enhance grain boundary sliding at the initial sintering stage by formation of hydroxyl ions [13]. Additionally, samples without the addition of water were SPS sintered as reference samples (SPS-FC-dry). Temperature control was provided by a thermocouple. The sintering experiments in the SPS machine were performed in vacuum. The samples were heated to 250 °C with a rate of 20 K/min and held for 20 min at a pressure of 400 MPa. Afterwards, the temperature was increased with a rate of 50 K/min up to 1050 °C and held for 20 min. During heating, the load was reduced to 150 MPa at 800 °C to prevent tool failure. The cooling rate was set to 100 K/min.

### 2.3. Sample characterization

The density after sintering was measured according to the Archimedes method. The phase compositions of all powders and sintered specimens were determined using a D4 Endeavor XRD device (Bruker, USA). SEM images were made using a Zeiss Ultra 55 SEM microscope (Carls Zeiss, Germany). Grain sizes were determined using the line intercept method on at least 350 grains for each sample. Scanning transmission electron microscopy (STEM) was utilized to characterize both SPS and conventionally sintered $SrTiO_3$ samples on a HF5000 S/TEM (Hitachi High-Technologies, Japan). High angle annular dark field (HAADF) imaging and energy dispersive X-ray spectroscopy (EDS) mappings were done for each sample. EDS maps were binned into linescans. The linescans then were quantified using a standardless method (Cliff-Lorimer), with k-factors calculated by assuming that the average composition of the EDS maps is equivalent to the nominal elemental composition of the material. EDS quantification and analysis was done using HyperSpy [52]. An error of at about 5% in the EDS results is expected due to the standardless quantification (which does not account for effects such as absorption and channeling) [53,54]. Samples for STEM characterization were prepared using a FEI Helios NanoLab 460F1 dual beam FIB/SEM, with a final milling energy of 2 kV [55]. Electrochemical impedance spectroscopy (EIS) analysis was performed using an Alpha-A high performance frequency analyzer (Novocontrol Technologies, Germany). Pt electrodes were burned in at 900 °C for 2 h. This heat treatment also assures equilibration of the oxygen vacancy concentration. The EIS measurements were performed between 650 °C and 400 °C in a frequency range of $10^{-1}$ Hz to $10^{6}$ Hz. For data analysis and fitting, the software RelaxIS (rhd instruments, Germany) was used. According to the brick-layer model, a series of RQ-circuits (a resistor connected in parallel to a constant phase element) was used as an equivalent circuit of the microstructure [56]. Distribution of relaxation times (DRT) analysis was performed with RelaxIS (rhd instruments, Germany) software to identify the necessary number of RQ-circuits in each equivalent circuit. In a DRT analysis, each electrochemical response of a sample (bulk or grain boundary; electric or ionic; electrode signal) shows a peak at its relaxation time. Each peak is then represented by one RQ-circuit in the equivalent circuit.

### 2.4. Calculation of space charge layer thickness, potential and conductivity

From fitting the impedance data, resistance and capacity values for the grain bulk and grain boundary were obtained. Space charge thicknesses $d_{SCL}$ were calculated according to the plate capacitor equation 1 [57–59]:

$$C = \epsilon_0 \epsilon_r \frac{A}{l} \tag{1}$$

where $C$ is the capacity, $\epsilon_0$ the permittivity of the vacuum, $\epsilon_r$ the relative permittivity of $SrTiO_3$ [40,48,60,61], $A$ the cross-sectional area and $l$ the sample thickness. The sample thickness is roughly equivalent to the number of grains across the sample thickness, $n$, multiplied with the grain size, $d_{grain}$. The number of grain boundaries across the sample thickness, $n-1$, is approximately $n$ for large values of $n$.

The capacity of a single grain boundary, $C_{GB,i}$, must be known to calculate the thickness of a single grain boundary. According to the brick-layer model, grain boundaries are assumed to be connected in series. $C_{GB,i}$ thereby can be calculated from the total grain boundary capacity, $C_{GB,total}$, which is the capacity of grain boundaries obtained from fitting the impedance data with an equivalent circuit:

$$\frac{1}{C_{GB,total}} = \sum_{1}^{n} \frac{1}{C_{GB,i}} = \frac{n}{C_{GB,i}} \tag{2}$$

The thickness of the space charge layer at the grain boundary $d_{SCL}$ can then be calculated by combining Equation 1 and 2 [62]:

$$d_{SCL} = \epsilon_0 \epsilon_r \cdot \frac{A}{n \cdot C_{GB,total}} \tag{3}$$

Similar to equation 3, the thickness of a grain can be obtained from the total grain capacity:

$$d_{grain} = \epsilon_0 \epsilon_r \cdot \frac{A}{n \cdot C_{bulk,total}} \tag{4}$$

Assuming identical relative permittivity within the grain and at the grain boundary, equations 3 and 4 result in a convenient way to calculate the grain boundary thickness, $d_{SCL}$, from the total bulk and grain boundary capacities [63]:

$$d_{SCL} = d_{grain} \cdot \frac{C_{bulk,total}}{C_{GB,total}} \tag{5}$$

For comparison, the Mott-Schottky model was used to calculate space charge layer widths as expected from the point defect concentrations as shown in equation 6 [39,64].

$$\lambda_{MS} = \lambda_{Debye} \cdot \sqrt{\frac{4e\Delta\Phi}{k_b T}} \tag{6}$$

where $\lambda_{Debye}$ is the Debye length of the space charge, $e$ the elementary charge, $\Delta\Phi$ the space charge potential, $k_b$ the Boltzman constant, T the temperature and $\lambda_{MS}$ the Mott-Schottky depletion layer width of the grain boundary. The Debye length has to be calculated according to equation 7 [39,65]:

$$\lambda_{Debye} = \sqrt{\frac{\epsilon_0 \epsilon_r k_b T}{2e^2 \cdot c_{major}}} \tag{7}$$

Here, $c_{major}$ is the concentration of major, mobile defects in $SrTiO_3$. Oxygen vacancies $V_O^{\cdot\cdot}$ and electron holes are the majority, mobile defects for conditions during impedance measurements (400–600 °C in air). The concentration of $V_O^{\cdot\cdot}$ is directly proportional to the (intrinsic) acceptor defect concentration in $SrTiO_3$ for the measurement conditions (see equation 8) [66] and is assumed to be in the range of $10^{18}$cm$^{-3}$.

$$[A^{'}] \approx 2[V_O^{\cdot\cdot}] \tag{8}$$

The concentration of electron holes is calculated using a mass action law derived from defect chemistry of $SrTiO_3$ (equation 9) [51,66,67]. There $K_P$ is the reaction constant, $[A_{Ti}^{'}]$ the concentration of acceptor defects and $P(O_2)$ the oxygen partial pressure during the measurement (0.21).

$$p = \left(\frac{K_p \cdot [A_{Ti}^{'}]}{2}\right)^{\frac{1}{2}} \cdot P(O_2)^{\frac{1}{4}} \tag{9}$$

The reaction constant $K_P(T)$is temperature dependent and is given by an Arrhenius law (equation 10) [51,67,68]. Here $K_{P0}$ is the reaction constant at $T = 0$K [67] and $\Delta H_{Ox}$ the oxidation enthalpy of $SrTiO_3$ assumed to be 1 eV [51].

$$K_P(T) = K_{P0} \cdot exp\left(-\frac{\Delta H_{Ox}}{k_B T}\right) \tag{10}$$

The space charge potential $\Delta\Phi$ is obtained by numerically solving equation 11 [64,69,70]. Finally, the space charge layer width can be calculated according to Mott-Schottky (equation 6).

$$\frac{\tau_{GB}}{\tau_{bulk}} = \frac{exp\left(\frac{e\Delta\Phi}{k_b T}\right)}{2e\Delta\Phi} \cdot k_b T \tag{11}$$

$\tau_{GB}$ and $\tau_{bulk}$ are the relaxation times of the grain boundary's and bulk's impedance signal. Grain boundary conductivities $\sigma_{GB}$ were calculated according to equation 12. $R_{GB,total}$ is the total grain boundary resistance obtained from fitting.

$$\sigma_{GB} = \frac{n \cdot d_{SCL}}{A \cdot R_{GB,total}} \tag{12}$$

The grain bulk conductivity $\sigma_{bulk}$ of SPS samples had to be calculated according to equation 13. For conventional sample the bulk conductivity was calculated without subtracting the total space charge thickness $n \cdot d_{scl}$ form the sample thickness $l$.

$$\sigma_{bulk} = \frac{l - n \cdot d_{SCL}}{A \cdot R_{bulk,total}} \tag{13}$$

## 3. Results and discussion

### 3.1. Sintering behavior

The relative densities of the SPS-NC and SPS-FC-dry samples are comparable to CS samples (Table 1). The SPS-PC and SPS-FC samples have slightly lower densities around 97%. Usually, $SrTiO_3$ is sintered at temperatures above 1300 °C to reach full densification. The high relative densities of SPS samples sintered at 1050 °C are achieved by applying high pressures (150–400 MPa) during SPS. The high pressure enables particle re-arrangement before sintering and grain boundary sliding during sintering [10]. Yet contrary to literature [10,13], water

**Table 1**
Relative densities of the sintered samples, depending on their sintering conditions. The first four samples were produced via SPS and the last sample by conventional processing.

| Powder | Sintering Temperature (°C) | Sintering Time (min) | Pressure (MPa) | Onset Temperature (°C) | Rel. Density (%) |
|---|---|---|---|---|---|
| SPS-NC | 250 & 1050 | 15 & 20 | 400 & 150 | 859 | 99.37 |
| SPS-PC | 250 & 1050 | 15 & 20 | 400 & 150 | 892 | 97.07 |
| SPS-FC | 250 & 1050 | 15 & 20 | 400 & 150 | 891 | 96.87 |
| SPS-FC-dry | 1050 | 20 | 400 & 150 | 893 | 99.76 |
| CS | 1425 | 60 | - | - | 99.10 |

does not seem to improve densification by grain sliding in the present case. The reference sample (SPS-FC-dry) sintered without water has the highest density of all samples, 2% higher than with water (SPS-FC). The addition of water before the SPS process also does not enable cold-sintering of $SrTiO_3$, likely due to its incongruent dissolution behavior, where $Sr^{2+}$ is preferentially solved in water [23,24]. The addition of water did not aid in densification at low temperature around 250 °C.

As evident from the sintering curves of SPS sintering (see supplementary Fig. S2), densification of SPS samples starts between 860 °C and 895 °C. The onset temperature of the SPS-FC and SPS-PC samples are comparable with one another. No improved densification for SPS-PC samples due to reactive sintering was observed with SPS-PC samples, possibly due to the low amount of precursor material inside the starting powder. The sintering onset temperature of the SPS-FC-dry sample is comparable to that of the SPS-FC sample, so its higher density may result from the absence of water in the powder.

The onset temperature of sintering decreases for the SPS-NC sample while its relative density increases. The improved sintering behavior is likely caused by the calcination reaction during sintering. The main driving force for sintering processes is the reduction of surface energy. Additional components can be the reduction of defect energy and the reduction of chemical potentials [8]. Chemical reactions, like the calcination reaction, generally reduce the chemical potential of components and provide additional driving force for the sintering process. The additional driving force added by the calcination reaction explains the enhanced sintering behavior of SPS-NC samples compared to the other SPS samples [8,15]. This also fits previous reports on enhanced densification rates during solid state reactive sintering [14,15].

### 3.2. SEM analysis of grain size

In Fig. 1, microstructures after CS and SPS sintering are shown. All samples have unimodal microstructure with average grain sizes not larger than 300 nm for SPS samples and 1.5 μm for CS $SrTiO_3$. The SPS samples' grain sizes are barely larger than the particle size of the used powders (100–300 nm, see supplementary Fig. S5). The small grain sizes of the SPS samples are a result of low grain boundary migration kinetics typical for low sintering temperatures [71].

It should be noted that the SPS-NC sample has slightly larger average grain size (275 nm) than SPS-PC or SPS-FC samples (252–256 nm). One possible explanation is the additional thermal energy released by the calcination reaction, which should be strongest in the SPS-NC sample. Another explanation is the smaller initial powder particle size of the SPS-NC powder (around 50 nm) enhancing the powder's sintering activity and leaving more time for grain growth after densification [9]. The average grain sizes of the CS and SPS samples are listed in Table 2.

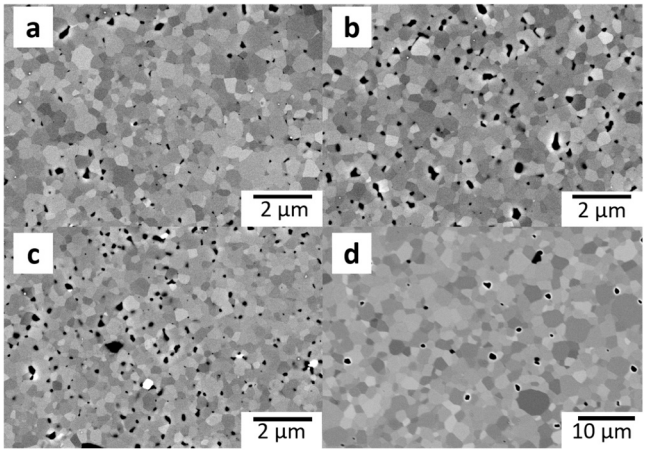


**Fig. 1.** SEM images of the microstructures of a) a SPS-NC sample, b) a SPS-PC sample, c) a SPS-FC sample and d) a CS $SrTiO_3$ sample.

All samples show Ti-rich secondary phase due to Zr abrasion introduced during milling. This is confirmed by the XRD-Results of the samples showing a small peak coinciding with $TiO_2$ (see supplementary Fig. S4). The SPS-NC samples clearly shows diffraction peaks of $TiO_2$, $SrCO_3$ and $SrTiO_3$. This suggests an incomplete calcination reaction. Microstructures of SPS-FC and SPS-PC samples show a large number of very small (<100 nm) intergranular pores, mirroring their relatively low densities (≈97%). These pores are also present in SPS-NC samples but are lower in number, as expected from the sintering behavior.

### 3.3. STEM analysis of grain boundary segregation

The different sintering conditions during SPS and conventional sintering are strongly impacting the microstructure formation (Fig. 1), and likely also grain boundary properties. To investigate the impact of sintering conditions on the grain boundary composition, the grain boundaries of a NC-SPS and a CS sample were analyzed using STEM-EDS. The mappings of two general grain boundaries are shown in Fig. 2. The CS sample has clear Ti segregation and Sr depletion at its grain boundary (Fig. 2a). No cationic segregation/depletion of Ti/Sr is observed at the grain boundary of the SPS sample (Fig. 2b). The segregation behavior becomes even clearer when looking at the corresponding integrated line scans shown in Fig. 3. The Ti and O concentration is increased, while the Sr concentration is strongly depleted at the grain boundary in the CS sample (Fig. 3a). In SPS samples, no segregation/depletion of Ti, O or Sr is observed (Figs. 2b, 3b). The change of oxygen and titanium concentration between the two grains in the SPS sample (Fig. 3b) is expected to be a result of channeling or thickness effects. At temperatures between 900 °C and 1200 °C, the diffusion speed of cationic defects is very low in $SrTiO_3$ [50,72]. Accordingly, the formation of an equilibrium space charge layer is not achievable within reasonable times for those temperatures [44,48,50,51]. We assume that the formation of an equilibrium space charge layer is kinetically inhibited during SPS sintering at 1050 °C with short sintering time and high cooling rates (100 K/min). Another explanation is the low oxygen partial pressure the samples are exposed to during SPS sintering. It is known that strontium vacancy concentration decreases (and oxygen vacancy concentration increases) in undoped $SrTiO_3$ for low oxygen partial pressure [36]. The changes in the bulk defect chemistry could reduce the space charge and result in little to no cationic defect segregation being observed.

It should be noted that even for conventional sintering, neutral grain boundaries with no segregation in $SrTiO_3$ do occur infrequently and are likely caused by grain boundary anisotropy [73,74]. A detailed statistical analysis will be necessary to reveal the impact of anisotropy on grain boundary segregation in Fig. 2 and Fig. 3.

### 3.4. Electrochemical characterization

To confirm our assumptions on the space charge layer, electrochemical impedance spectroscopy (EIS) was used to characterize the electrical GB properties after SPS sintering. Fig. 4 contains normalized impedance plots of the SPS and CS samples and show that the total impedance of SPS samples is higher than that of CS samples. The CS sample's impedance plot consists of two semi-circles, i.e. one small semi-circle that is visible at the high frequency part of the impedance plot and one large, slightly distorted semi-circle at the mid to low frequency range. The small semi-circle most likely represents the grain bulk of the CS sample, while the larger distorted semi-circle represents the

**Table 2**
Average grain sizes of SPS and conventionally sintered $SrTiO_3$ samples. The standard error of the average grain size is added.

| Sample | CS | SPS-FC | SPS-PC | SPS-NC |
|---|---|---|---|---|
| Average grain size (nm) | 1540 ± 36 | 252 ± 8 | 257 ± 8 | 275 ± 10 |

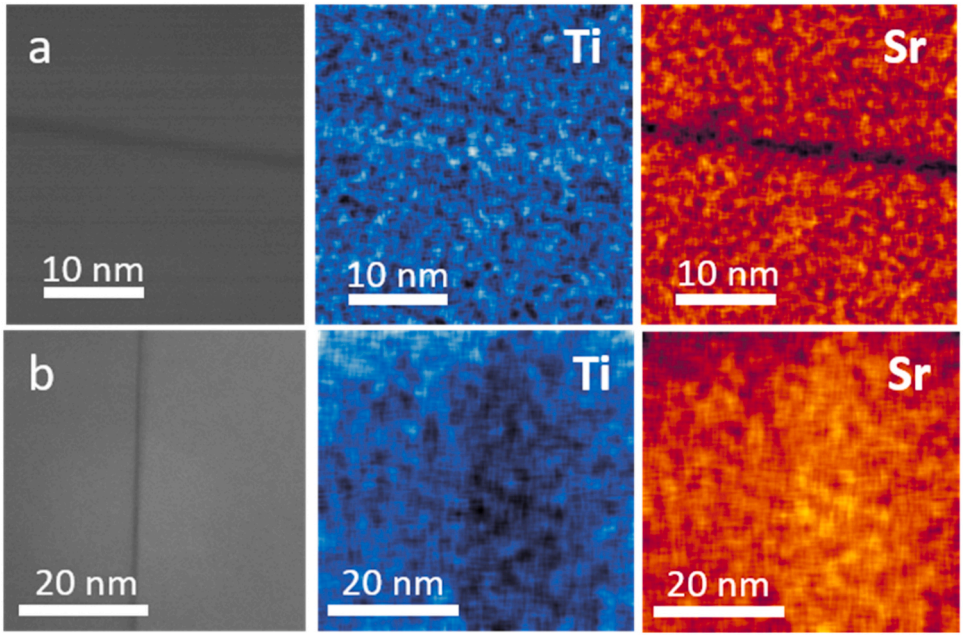


**Fig. 2.** Dark field images and EDS mappings of Ti and Sr at a grain boundary in a) conventionally sintered $SrTiO_3$ and b) SPS sintered $SrTiO_3$.

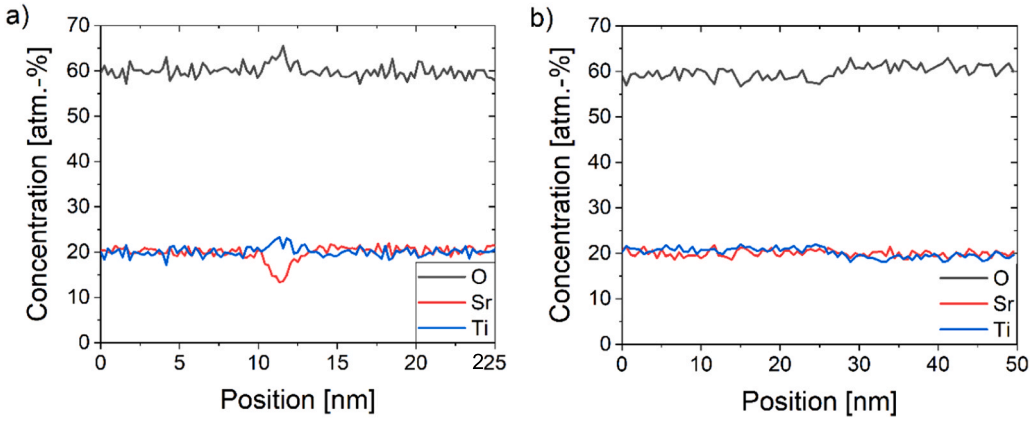


**Fig. 3.** Integrated EDS line scan of the grain boundaries in Fig. 2. A) line scan of a CS sample and b) line scan of a SPS-NC sample are depicted. The concentration of elements is given in atom-%.

dispersed grain boundary response of the CS sample. The distortion of the grain boundary semi-circle in impedance plots of $SrTiO_3$ was previously reported in literature [62]. For SPS sintered samples, the impedance plots consist of only one large, broadened semi-circle.

According to DRT, there is more than one electrochemical response with very different relaxation times present in SPS samples (see supplementary Fig. S7). It can be excluded that one of these relaxation times correlates to the Pt electrodes, because any electrical response of the electrodes would be very low in signal and mostly hidden in noise of the impedance plots' low frequency part (right-hand side of Fig. 4). Such minor electrode responses are typical for Pt or Ag electrodes on $SrTiO_3$ samples. [59,75].

Impedance data of the CS and SPS samples were fitted with a series of RQ-circuits according to the brick-layer model. Based on the DRT results, the equivalent circuit of SPS and CS samples used a series of 2 RQ circuits. For both sample types one RQ circuit represents the samples' bulk response while the other represents the grain boundary response. It should be noted that the grain boundary response of SPS (well visible in the modulus plot, see supplementary Fig. S8) is only partially resolved by the frequency range of measurement, which could lead to later fitting errors.

The fitting results (see supplementary Table S2) were used to calculate space charge potentials as well as space charge thickness according to the Mott-Schottky model (Equation 6) and the plate capacitor equation (Equation 3). Capacity values of the CS samples fit the expected values of $2.1 \cdot 10^{-11}$ F for bulk and $10^{10}$ F to $10^{-8}$ F for grain boundaries (Table 3) [63]. Space charge thicknesses calculated by the plate capacitor equation are in the range of 41 nm (650 °C) to 103 nm (525 °C) depending on measuring temperature. Space charge thicknesses calculated according to the Mott-Schottky model change less with temperature and range between 75 nm (650 °C) and 100 nm (525 °C). In this model, The change in space charge thickness with temperature is due to an increase of overall defect concentration with increasing temperature [51,60,66,76,77]. Calculated space charge thicknesses of CS samples agree with values reported in literature, ranging from 5 nm to 100 nm in $SrTiO_3$ [39,59,78].

Capacity values of the SPS samples range from $10^{-11}$ F to $10^{-10}$ F for both bulk and grain boundary. Surprisingly, the grain bulk capacity is larger than the GB capacity in SPS samples. The space charge thicknesses of SPS samples calculated with the plate capacitor equation increase

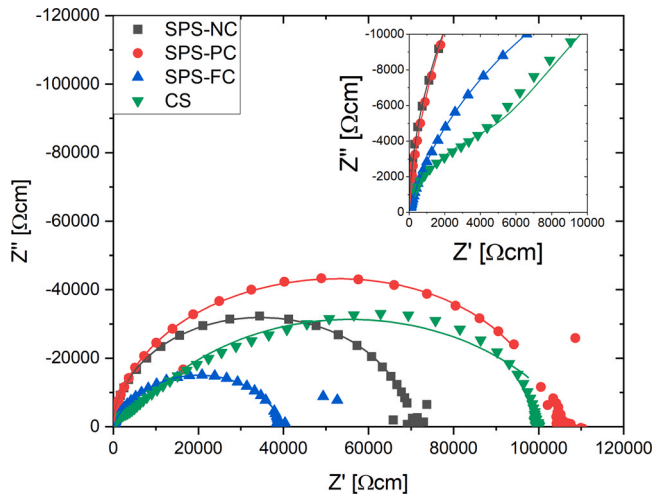


**Fig. 4.** Impedance-plots of the SPS & CS samples measured at 600 °C. The impedance plots are normalized to the sample dimension. The colored lines represent standardized fits of the respective raw data.

**Table 3**
Space charge layer thickness calculated according to the Plate capacitor equation and Mott-Schottky Model, as well as the space charge potential at the grain boundary. These values were calculated for the measurement temperature of 550 °C.

| Sample | Plate capacitor (nm) | Mott-Schottky (nm) | Space charge potential (V) |
|---|---|---|---|
| CS (air) | 55 | 91 | 0.35 |
| SPS-NC | 35 | 51 | 0.11 |
| SPS-PC | 26 | 53 | 0.12 |
| SPS-FC | 13 | 61 | 0.16 |

from 13 nm to 84 nm as the degree of powder calcination was reduced from fully calcined to non-calcined. Contrary to that, space charge thicknesses calculated according to the Mott-Schottky model decrease from 61 nm to 51 nm as the degree of powder calcination was reduced. Space charge layer thicknesses of SPS samples also fit the size range reported in literature [39,59,78]. There is no clear explanation for the differences between space charge thicknesses obtained from the plate capacitor equation and the Mott-Schottky model. This can be an artefact resulting from the fitting process since the grain bulk response is not fully resolved by measurement's frequency range (see modulus data in supplementary Fig. S8). Additionally, the bulk signal diminishes in strength as the grain size of $SrTiO_3$ decreases, until a critical grain size is reached below which only the grain boundary signal is measurable. This has been correlated to the increasing volume fraction the space charge layer covers in grains with decreasing grain size [65,79]. Also, investigating the different space charge models reveals that the Mott-Schottky model overestimated the real space charge thickness [80].

The space charge potential of the CS samples (0.35 V) fits previous reports, which range from 0.3 V to 0.7 V [43,64]. Space charge potentials of SPS samples are much smaller, ranging from 0.11 V to 0.16 V (Table 3). Since the segregation of point defects towards grain boundaries is necessary for the formation of space charge layers, the low space charge in SPS samples indicates a low defect concentration at the grain boundary core relative to the bulk [44,81–83]. This agrees with observation of the STEM-EDS mappings (Fig. 2 and Fig. 3), where little to no cationic segregation was observed at GB of the SPS sample (Fig. 2b). One possible explanation is the inhibited segregation of strontium vacancies and titanium ions due to the low sintering temperatures and short times during SPS experiments. Only defects of high mobility (oxygen vacancies and electron holes) are able to segregate towards the grain boundary resulting in a lower space charge potential in the SPS samples. Another explanation is the reducing atmosphere during SPS sintering. It is known, that the strontium vacancy concentration in undoped $SrTiO_3$ is reduced with decreasing oxygen partial pressure [36]. Due to the high bulk concentration of oxygen vacancies and few strontium vacancies that could segregate towards grain boundaries the space charge width and the space charge potential decrease (space charge widths and potentials calculated from impedance data of reduced samples show similar results to the SPS sintered samples; see supplementary Table S2).

The reduction in space charge thickness and potential seen in the SPS samples also seem to influence the samples' conductivities. When looking at Fig. 5 the specific grain boundary and total conductivity of CS and SPS samples are comparable with the grain boundary conductivity being slightly higher in SPS samples than in CS samples. The bulk conductivity is lower in SPS-NC and SPS-PC samples than in CS samples, but this can also be an artefact of the calculation method used (see equation 13). Overall conductivites of SPS and CS samples are comparable with the SPS samples having higher conductivites than the CS samples at lower temperatures ($\leq$ 550 °C). A better indication for the impact of space charge potential on the grain boundary conductivity seem to be activation energy. Table 4 lists the activation energy for grain boundary conduction in CS and SPS samples. The activation energies were obtained by fitting an Arrhenius law to the conductivity plots of Fig. 5.

The activation energies are around 1.5–1.6 eV for SPS samples, while the activation energy for grain boundary conduction in CS samples is around 2.7 eV. This difference could stem from the lower space charge potential at the SPS samples' grain boundaries as this should ease the charge transport across grain boundaries. The difference could also be explained by changes in the SPS samples introduced by the processing method. Overall charge transport across grain boundaries in SPS samples seems to need less energy than in CS samples.

## 4. Summary and conclusion

High-pressure SPS of $SrTiO_3$ could generate highly dense ceramic materials with sub-micron grain sizes (250–275 nm). The slightly higher density and grain sizes of ceramics made from precursor powder mixtures result from a reactive sintering process during the SPS sintering. XRD results indicate that the calcination reaction during spark plasma sintering (SPS) was incomplete. In contrast to conventionally sintered samples, SPS samples show no cationic segregation at their grain boundaries. Low sintering temperature and short sintering times prevented cationic segregation due to low cationic vacancy mobility. Impedance data indicate the presence of space charge layer in conventionally sintered and SPS samples that reach the expected thickness of 5–100 nm for undoped $SrTiO_3$ ceramics. The space charge layer most likely only consists of mobile charge carrier such as oxygen vacancies and electron holes. The low defect segregation at the grain boundary causes low space charge potentials in SPS samples. The lower space charge potential at grain boundaries affect the grain boundary conductivity of SPS samples positively. The lower electric potential barrier at the grain boundary reduces the activation energy of charge transport across grain boundaries in SPS samples and slightly increases the grain boundary conductivity of SPS samples. The overall conductivity of SPS is comparable to that of CS samples.

The current paper has shown that FAST/SPS sintering has the potential to produce dense ceramics materials comparable to conventional sintering methods at temperatures well below conventional sintering. Combining the FAST/SPS sintering method with solid state reactive sintering (SSRS) can further decrease sintering temperatures and still result in high-quality microstructures. Beyond microstructures, FAST/SPS sintering offers a unique pathway for grain boundary engineering as the combination of reducing sintering conditions, low sintering temperature and fast heating/cooling rates prevent the formation of space charge layers. Consequently, very high grain boundary conductivity can be achieved, which is beneficial for applications of ionic conductors for SOFC and similar applications.

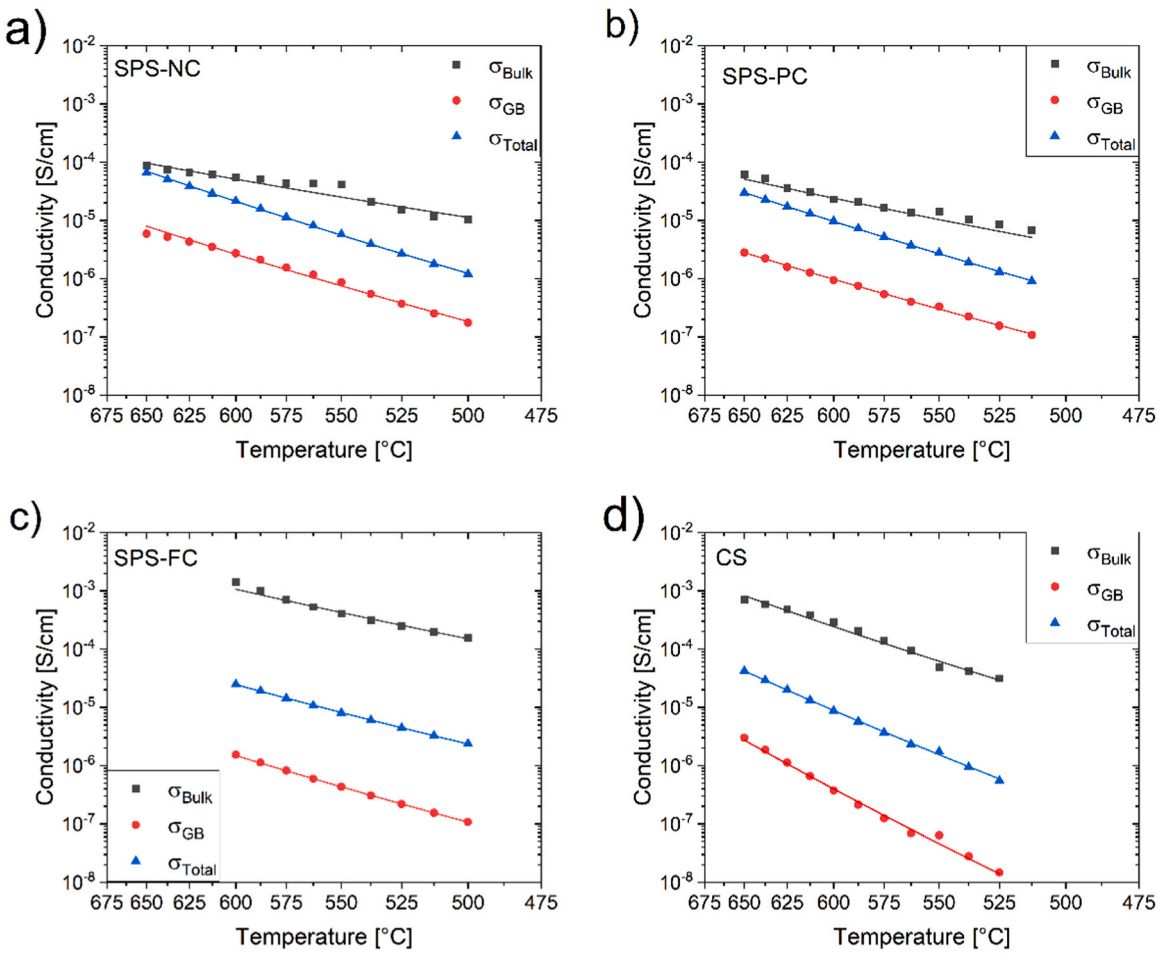


**Fig. 5.** Bulk, grain boundary and total conductivity of a) SPS-NC, b) SPS-PC, c) SPS-FC and d) CS samples. The straight lines represent fits of the data with an Arrhenius law.

**Table 4**
Activation energy of grain boundary conduction (GB) for SPS and conventionally sintered samples.

| Sample | SPS-NC | SPS-PC | SPS-FC | CS-Ox. |
|---|---|---|---|---|
| Activation Energy GB (eV) | 1.6 | 1.5 | 1.5 | 2.7 |

## Declaration of Competing Interest

The authors declare that they have no known competing financial interests or personal relationships that could have appeared to influence the work reported in this paper.

## Acknowledgments

The authors acknowledge funding by the DFG under MA 1280/69–1 (OG, MK) and via the Emmy Noether Programme under contract No. Rh 146/1-1 (WR, MPZ, DJ). The authors acknowledge the support of Hitachi High-Technologies in providing access to and expertise for the HF5000 STEM.

## Appendix A. Supporting information

Supplementary data associated with this article can be found in the online version at doi:10.1016/j.jeurceramsoc.2023.07.021.

## References

[1] O. Guillon, R.A. De Souza, T.P. Mishra, W. Rheinheimer, Electric-field-assisted processing of ceramics: nonthermal effects and related mechanisms, MRS Bull. 46 (2021) 52–58, https://doi.org/10.1557/s43577-020-00008-w.
[2] Z.-Y. Hu, Z.-H. Zhang, X.-W. Cheng, F.-C. Wang, Y.-F. Zhang, S.-L. Li, A review of multi-physical fields induced phenomena and effects in spark plasma sintering: fundamentals and applications, Mater. Des. 191 (2020), 108662, https://doi.org/10.1016/j.matdes.2020.108662.
[3] M. Bram, A.M. Laptev, T.P. Mishra, K. Nur, M. Kindelmann, M. Ihrig, J.G. Pereira Da Silva, R. Steinert, H.P. Buchkremer, A. Litnovsky, F. Klein, J. Gonzalez-Julian, O. Guillon, Application of electric current-assisted sintering techniques for the processing of advanced materials, Adv. Eng. Mater. 22 (2020) 2000051, https://doi.org/10.1002/adem.202000051.
[4] O. Guillon, J. Gonzalez-Julian, B. Dargatz, T. Kessel, G. Schierning, J. Räthel, M. Herrmann, Field-assisted sintering technology/spark plasma sintering: mechanisms, materials, and technology developments, Adv. Eng. Mater. 16 (2014) 830–849, https://doi.org/10.1002/adem.201300409.
[5] M. Suarez, A. Fernandez, J.L. Menendez, R. Torrecillas, H. U, J. Hennicke, R. Kirchner, T. Kessel, Challenges and Opportunities for Spark Plasma Sintering: A Key Technology for a New Generation of Materials, in: B. Ertug (Ed.), Sintering Applications, InTech, 2013, https://doi.org/10.5772/53706.
[6] Z. Shen, M. Nygren, Microstructural prototyping of ceramics by kinetic engineering: applications of spark plasma sintering, Chem. Rec. 5 (2005) 173–184, https://doi.org/10.1002/tcr.20043.
[7] M.N. Rahaman, R. Manalert, Grain boundary mobility of $BaTiO_3$ doped with aliovalent cations, J. Eur. Ceram. Soc. 18 (1998) 1063–1071, https://doi.org/10.1016/S0955-2219(97)00215-X.
[8] R. Telle, H. Salmang, H. Scholze, Keramik, 7., vollst. neubearb. und erw (eds.), Aufl, Springer, Berlin, 2007.
[9] J. Langer, M.J. Hoffmann, O. Guillon, Electric field-assisted sintering and hot pressing of semiconductive zinc oxide: a comparative study: fast sintering and hot pressing of semiconductive zinc oxide, J. Am. Ceram. Soc. 94 (2011) 2344–2353, https://doi.org/10.1111/j.1551-2916.2011.04396.x.

[10] R. Chaim, Z. Shen, M. Nygren, Transparent nanocrystalline MgO by rapid and low-temperature spark plasma sintering, J. Mater. Res. 19 (2004) 2527–2531, https://doi.org/10.1557/JMR.2004.0334.

[11] C.P. Cameron, R. Raj, Grain-growth transition during sintering of colloidally prepared alumina powder compacts, J. Am. Ceram. Soc. 71 (1988) 1031–1035, https://doi.org/10.1111/j.1151-2916.1988.tb05787.x.

[12] R.L. Coble, Sintering Crystalline Solids. I. Intermediate and Final State Diffusion Models, J. Appl. Phys. 32 (1961) 787–792, https://doi.org/10.1063/1.1736107.

[13] J.-L. Hebrard, P. Nortier, M. Pijolat, M. Soustelle, Initial sintering of submicrometer titania anatase powder, J. Am. Ceram. Soc. 73 (1990) 79–84, https://doi.org/10.1111/j.1151-2916.1990.tb05094.x.

[14] H. Juang, Effect of calcination on sintering of hydroxyapatite, Biomaterials 17 (1996) 2059–2064, https://doi.org/10.1016/0142-9612(96)88882-X.

[15] S. Bresch, Influence of reaction-sintering and calcination conditions on thermoelectric properties of sm-doped calcium manganate $CaMnO_3$, J. ceram, Sci. Technol. (2018), https://doi.org/10.4416/JCST2018-00017.

[16] P. Barai, T. Fister, Y. Liang, J. Libera, M. Wolfman, X. Wang, J. Garcia, H. Iddir, V. Srinivasan, Investigating the Calcination and Sintering of $Li_7La_3Zr_2O_{12}$ (LLZO) Solid Electrolytes Using Operando Synchrotron X-ray Characterization and Mesoscale Modeling, Chem. Mater. 33 (2021) 4337–4352, https://doi.org/10.1021/acs.chemmater.0c04393.

[17] J. Tong, D. Clark, L. Bernau, M. Sanders, R. O'Hayre, Solid-state reactive sintering mechanism for large-grained yttrium-doped barium zirconate proton conducting ceramics, J. Mater. Chem. 20 (2010) 6333, https://doi.org/10.1039/c0jm00381f.

[18] J. Tong, D. Clark, L. Bernau, A. Subramaniyan, R. O'Hayre, Proton-conducting yttrium-doped barium cerate ceramics synthesized by a cost-effective solid-state reactive sintering method, Solid State Ion. 181 (2010) 1486–1498, https://doi.org/10.1016/j.ssi.2010.08.022.

[19] J. Tong, D. Clark, M. Hoban, R. O'Hayre, Cost-effective solid-state reactive sintering method for high conductivity proton conducting yttrium-doped barium zirconium ceramics, Solid State Ion. 181 (2010) 496–503, https://doi.org/10.1016/j.ssi.2010.02.008.

[20] M. Kindelmann, J.N. Ebert, W.S. Scheld, W. Deibert, W.A. Meulenberg, W. Rheinheimer, M. Bram, J. Mayer, O. Guillon, Cold sintering of $BaZr_{0.7}Ce_{0.2}Y_{0.1}O_{3-\delta}$ ceramics by controlling the phase composition of the starting powders, Scr. Mater. 224 (2023), 115147, https://doi.org/10.1016/j.scriptamat.2022.115147.

[21] T. Sada, Z. Fan, A. Ndayishimiye, K. Tsuji, S.H. Bang, Y. Fujioka, C.A. Randall, In situ doping of $BaTiO_3$ and visualization of pressure solution in flux-assisted cold sintering, J. Am. Ceram. Soc. 104 (2021) 96–104, https://doi.org/10.1111/jace.17461.

[22] R. Boston, J. Guo, S. Funahashi, A.L. Baker, I.M. Reaney, C.A. Randall, Reactive intermediate phase cold sintering in strontium titanate, RSC Adv. 8 (2018) 20372–20378, https://doi.org/10.1039/C8RA03072C.

[23] J. Andrews, D. Button, I.M. Reaney, Advances in cold sintering: improving energy consumption and unlocking new potential in component manufacturing, Johns. Matthey Technol. Rev. 64 (2020) 219–232, https://doi.org/10.1595/205651320X15814150061554.

[24] H. Guo, A. Baker, J. Guo, C.A. Randall, Cold sintering process: a novel technique for low-temperature ceramic processing of ferroelectrics, J. Am. Ceram. Soc. 99 (2016) 3489–3507, https://doi.org/10.1111/jace.14554.

[25] S. Grasso, M. Biesuz, L. Zoli, G. Taveri, A.I. Duff, D. Ke, A. Jiang, M.J. Reece, A review of cold sintering processes, Adv. Appl. Ceram. 119 (2020) 115–143, https://doi.org/10.1080/17436753.2019.1706825.

[26] M. Bäurer, H. Kungl, M.J. Hoffmann, Influence of Sr/Ti stoichiometry on the densification behavior of strontium titanate, J. Am. Ceram. Soc. 92 (2009) 601–606, https://doi.org/10.1111/j.1551-2916.2008.02920.x.

[27] T.P. Mishra, S. Wang, C. Lenser, D. Jennings, M. Kindelmann, W. Rheinheimer, C. Broeckmann, M. Bram, O. Guillon, Ultra-fast high-temperature sintering of strontium titanate, Acta Mater. 231 (2022), 117918, https://doi.org/10.1016/j.actamat.2022.117918.

[28] F. Lemke, W. Rheinheimer, M.J. Hoffmann, A comparison of power controlled flash sintering and conventional sintering of strontium titanate, Scr. Mater. 130 (2017) 187–190, https://doi.org/10.1016/j.scriptamat.2016.12.008.

[29] K. Naik, S.K. Jha, R. Raj, Correlations between conductivity, electroluminescence and flash sintering, Scr. Mater. 118 (2016) 1–4, https://doi.org/10.1016/j.scriptamat.2016.03.001.

[30] W. Rheinheimer, X.L. Phuah, L. Porz, M. Scherer, J. Cho, H. Wang, The impact of flash sintering on densification and plasticity of strontium titanate: High heating rates, dislocation nucleation and plastic flow, J. Eur. Ceram. Soc. 43 (2023) 3524–3537, https://doi.org/10.1016/j.jeurceramsoc.2023.02.007.

[31] W. Rheinheimer, X.L. Phuah, H. Wang, F. Lemke, M.J. Hoffmann, H. Wang, The role of point defects and defect gradients in flash sintering of perovskite oxides, Acta Mater. 165 (2019) 398–408, https://doi.org/10.1016/j.actamat.2018.12.007.

[32] L. Porz, M. Scherer, D. Huhn, L.-M. Heine, S. Britten, L. Rebohle, M. Neubert, M. Brown, P. Lascelles, R. Kitson, D. Rettenwander, L. Fulanovic, E. Bruder, P. Breckner, D. Isaia, T. Frömling, J. Rödel, W. Rheinheimer, Blacklight sintering of ceramics, Mater. Horiz. 9 (2022) 1717–1726, https://doi.org/10.1039/D2MH00177B.

[33] T.T. Khan, I.-H. Kim, S.-C. Ur, Improvement of the Thermoelectric Properties of the Perovskite $SrTiO_3$ by Cr-Doping, J. Elec Mater. 48 (2019) 1864–1869, https://doi.org/10.1007/s11664-018-6623-9.

[34] M. Ito, T. Matsuda, Thermoelectric properties of non-doped and Y-doped $SrTiO_3$ polycrystals synthesized by polymerized complex process and hot pressing, J. Alloy. Compd. 477 (2009) 473–477, https://doi.org/10.1016/j.jallcom.2008.10.031.

[35] C. Bae, J.-G. Park, Y.-H. Kim, H. Jeon, Abnormal grain growth of niobium-doped strontium titanate ceramics, J. Am. Ceram. Soc. 81 (2005) 3005–3009, https://doi.org/10.1111/j.1151-2916.1998.tb02727.x.

[36] F. Lemke, W. Rheinheimer, M.J. Hoffmann, Sintering and grain growth in $SrTiO_3$: impact of defects on kinetics, J. Ceram. Soc. Jpn. 124 (2016) 346–353, https://doi.org/10.2109/jcersj2.15265.

[37] S.-Y. Chung, D.Y. Yoon, S.-J.L. Kang, Effects of donor concentration and oxygen partial pressure on interface morphology and grain growth behavior in $SrTiO_3$, Acta Mater. 50 (2002) 3361–3371, https://doi.org/10.1016/S1359-6454(02)00139-8.

[38] W. Rheinheimer, M.J. Hoffmann, Grain growth in perovskites: what is the impact of boundary transitions? Curr. Opin. Solid State Mater. Sci. 20 (2016) 286–298, https://doi.org/10.1016/j.cossms.2016.04.004.

[39] G. Gregori, R. Merkle, J. Maier, Ion conduction and redistribution at grain boundaries in oxide systems, Prog. Mater. Sci. 89 (2017) 252–305, https://doi.org/10.1016/j.pmatsci.2017.04.009.

[40] M. Vollmann, R. Hagenbeck, R. Waser, Grain-boundary defect chemistry of acceptor-doped titanates: inversion layer and low-field conduction, J. Am. Ceram. Soc. 80 (1997) 2301–2314, https://doi.org/10.1111/j.1151-2916.1997.tb03121.x.

[41] Y.-M. Chiang, T. Takagi, Grain-boundary chemistry of barium titanate and strontium titanate: i, high-temperature equilibrium space charge, J. Am. Ceram. Soc. 73 (1990) 3278–3285, https://doi.org/10.1111/j.1151-2916.1990.tb06450.x.

[42] Y.-M. Chiang, T. Takagi, Grain-boundary chemistry of barium titanate and strontium titanate: II, origin of electrical barriers in positive-temperature-coefficient thermistors, J. Am. Ceram. Soc. 73 (1990) 3286–3291, https://doi.org/10.1111/j.1151-2916.1990.tb06451.x.

[43] R.A.D. Souza, J. Fleig, R. Merkle, J. Maier, $SrTiO_3$: a model electroceramic, Int. J. Mater. Res. 94 (2003) 218–225, https://doi.org/10.3139/ijmr-2003-0043.

[44] R.A.De Souza, The formation of equilibrium space-charge zones at grain boundaries in the perovskite oxide $SrTiO_3$, Phys. Chem. Chem. Phys. 11 (2009) 9939, https://doi.org/10.1039/b904100a.

[45] J. Maier, Ionic conduction in space charge regions, Prog. Solid State Chem. 23 (1995) 171–263, https://doi.org/10.1016/0079-6786(95)00004-E.

[46] A. Tschope, S. Kilassonia, R. Birringer, The grain boundary effect in heavily doped cerium oxide, Solid State Ion. 173 (2004) 57–61, https://doi.org/10.1016/j.ssi.2004.07.052.

[47] A. Tschöpe, Interface Defect Chemistry and Effective Conductivity in Polycrystalline Cerium Oxide, J. Electroceram 14 (2005) 5–23, https://doi.org/10.1007/s10832-005-6580-6.

[48] R. Hagenbeck, R. Waser, Influence of temperature and interface charge on the grain-boundary conductivity in acceptor-doped $SrTiO_3$ ceramics, J. Appl. Phys. 83 (1998) 2083–2092, https://doi.org/10.1063/1.366941.

[49] X. Guo, Physical origin of the intrinsic grain-boundary resistivity of stabilized-zirconia: Role of the space-charge layers, Solid State Ion. 81 (1995) 235–242, https://doi.org/10.1016/0167-2738(95)00180-E.

[50] F. Gunkel, R. Waser, A.H.H. Ramadan, R.A. De Souza, S. Hoffmann-Eifert, R. Dittmann, Space charges and defect concentration profiles at complex oxide interfaces, Phys. Rev. B. 93 (2016), 245431, https://doi.org/10.1103/PhysRevB.93.245431.

[51] R. Moos, K.H. Haerdtl, Defect Chemistry of Donor-Doped and Undoped Strontium Titanate Ceramics between 1000° and 1400°C, J. Am. Ceram. Soc. 80 (2005) 2549–2562, https://doi.org/10.1111/j.1151-2916.1997.tb03157.x.

[52] F. De La Peña, E. Prestat, V.T. Fauske, P. Burdet, J. Lähnemann, P. Jokubauskas, T. Furnival, M. Nord, T. Ostasevicius, K.E. MacArthur, D.N. Johnstone, M. Sarahan, J. Taillon, T. Aarholt, Pquinn-Dls, V. Migunov, A. Eljarrat, J. Caron, C. Francis, T. Nemoto, T. Poon, S. Mazzucco, Actions-User, N. Tappy, N. Cautaerts, Suhas Somnath, T. Slater, M. Walls, F. Winkler, H.W. Ånes, hyperspy/hyperspy: Release v1.7.2, (2022). ⟨https://doi.org/10.5281/ZENODO.7090040⟩.

[53] D.E. Newbury, N.W.M. Ritchie, Is Scanning Electron Microscopy/Energy Dispersive X-ray Spectrometry (SEM/EDS) Quantitative?: Quantitative SEM/EDS analysis, Scanning 35 (2013) 141–168, https://doi.org/10.1002/sca.21041.

[54] H. Hoeft, P. Schwaab, Investigations towards optimizing EDS analysis by the Cliff-Lorimer method in scanning transmission electron microscopy, X-Ray Spectrom. 17 (1988) 201–208, https://doi.org/10.1002/xrs.1300170509.

[55] M. Kruth, D. Meertens, K. Tillmann, FEI Helios NanoLab 460F1 FIB-SEM, JLSRF 2 (2016) A59, https://doi.org/10.17815/jlsrf-2-105.

[56] J.E. Bauerle, Study of solid electrolyte polarization by a complex admittance method, J. Phys. Chem. Solids 30 (1969) 2657–2670, https://doi.org/10.1016/0022-3697(69)90039-0.

[57] S.M. Haile, D.L. West, J. Campbell, The role of microstructure and processing on the proton conducting properties of gadolinium-doped barium cerate, J. Mater. Res. 13 (1998) 1576–1595, https://doi.org/10.1557/JMR.1998.0219.

[58] T. Van Dijk, A.J. Burggraaf, Grain boundary effects on ionic conductivity in ceramic $Gd_xZr_{1-x}O_{2-(x/2)}$ solid solutions, Phys. Stat. Sol. (a). 63 (1981) 229–240, https://doi.org/10.1002/pssa.2210630131.

[59] I. Denk, J. Claus, J. Maier, Electrochemical Investigations of $SrTiO_3$ Boundaries, J. Electrochem. Soc. 144 (1997) 3526–3536, https://doi.org/10.1149/1.1838044.

[60] M. Vollman, R. Waser, Grain boundary defect chemistry of acceptor-doped titanates: space charge layer width, J. Am. Ceram. Soc. 77 (1994) 235–243, https://doi.org/10.1111/j.1151-2916.1994.tb06983.x.

[61] R. Hagenbeck, R. Waser, Detailed temperature dependence of the space charge layer width at grain boundaries in acceptor-doped $SrTiO_3$-ceramics, J. Eur. Ceram. Soc. 19 (1999) 683–686, https://doi.org/10.1016/S0955-2219(98)00296-9.

[62] J.C.C. Abrantes, J.A. Labrincha, J.R. Frade, Applicability of the brick layer model to describe the grain boundary properties of strontium titanate ceramics, J. Eur.

Ceram. Soc. 20 (2000) 1603–1609, https://doi.org/10.1016/S0955-2219(00)00022-4.
[63] J.T.S. Irvine, D.C. Sinclair, A.R. West, Electroceramics: characterization by impedance spectroscopy, Adv. Mater. 2 (1990) 132–138, https://doi.org/10.1002/adma.19900020304.
[64] J. Fleig, The grain boundary impedance of random microstructures: numerical simulations and implications for the analysis of experimental data, Solid State Ion. 150 (2002) 181–193, https://doi.org/10.1016/S0167-2738(02)00274-6.
[65] P. Balaya, J. Jamnik, J. Fleig, J. Maier, Mesoscopic electrical conduction in nanocrystalline $SrTiO_3$, Appl. Phys. Lett. 88 (2006), 062109, https://doi.org/10.1063/1.2171798.
[66] D.M. Smyth, The defect chemistry of metal oxides, Oxford University Press,, New York, 2000.
[67] M. Fleischer, H. Meixner, C. Tragut, Hole Mobility in Acceptor-Doped, Monocrystalline $SrTiO_3$, J. Am. Ceram. Soc. 75 (1992) 1666–1668, https://doi.org/10.1111/j.1151-2916.1992.tb04242.x.
[68] I. Denk, W. Münch, J. Maier, Partial Conductivities in $SrTiO_3$: Bulk Polarization Experiments, Oxygen Concentration Cell Measurements, and Defect-Chemical Modeling, J. Am. Ceram. Soc. 78 (1995) 3265–3272, https://doi.org/10.1111/j.1151-2916.1995.tb07963.x.
[69] J. Fleig, S. Rodewald, J. Maier, Microcontact impedance measurements of individual highly resistive grain boundaries: General aspects and application to acceptor-doped $SrTiO_3$, J. Appl. Phys. 87 (2000) 2372–2381, https://doi.org/10.1063/1.372189.
[70] S. Rodewald, J. Fleig, J. Maier, Microcontact impedance spectroscopy at single grain boundaries in Fe-doped $SrTiO_3$ polycrystals, J. Am. Ceram. Soc. 84 (2001) 521–530, https://doi.org/10.1111/j.1151-2916.2001.tb00693.x.
[71] W. Rheinheimer, M.J. Hoffmann, Non-Arrhenius behavior of grain growth in strontium titanate: new evidence for a structural transition of grain boundaries, Scr. Mater. 101 (2015) 68–71, https://doi.org/10.1016/j.scriptamat.2015.01.021.
[72] T. Bieger, H. Yugami, N. Nicoloso, J. Maier, R. Waser, Optical absorption relaxation applied to $SrTiO_3$ and $ZrO_2$: An in-situ method to study trapping effects on chemical diffusion, Solid State Ion. 72 (1994) 41–46, https://doi.org/10.1016/0167-2738(94)90122-8.
[73] S.-J. Shih, S. Lozano-Perez, D.J.H. Cockayne, Investigation of grain boundaries for abnormal grain growth in polycrystalline $SrTiO_3$, J. Mater. Res. 25 (2010) 260–265, https://doi.org/10.1557/JMR.2010.0046.
[74] M. Bäurer, S.-J. Shih, C. Bishop, M.P. Harmer, D. Cockayne, M.J. Hoffmann, Abnormal grain growth in undoped strontium and barium titanate, Acta Mater. 58 (2010) 290–300, https://doi.org/10.1016/j.actamat.2009.09.007.
[75] X. Guo, J. Fleig, J. Maier, Separation of electronic and ionic contributions to the grain boundary conductivity in acceptor-doped $SrTiO_3$, J. Electrochem. Soc. 148 (2001) J50, https://doi.org/10.1149/1.1389344.
[76] R.E. Howard, A.B. Lidiard, Matter transport in solids, Rep. Prog. Phys. 27 (1964) 161–240, https://doi.org/10.1088/0034-4885/27/1/305.
[77] P. Debye, E. Hückel, Zur Theorie der Elektrolyte. I. Gefrierpunktserniedrigung und verwandte Erscheinungen, Phys. Z. 24 (1923) 305.
[78] S.K. Rout, J. Bera, Grain and grain-boundary study of acceptor doped $SrTiO_3$ ceramics using impedance spectroscopy, Ferroelectrics 323 (2005) 79–84, https://doi.org/10.1080/00150190500308777.
[79] P. Lupetin, G. Gregori, J. Maier, Mesoscopic charge carriers chemistry in nanocrystalline $SrTiO_3$, Angew. Chem. 122 (2010) 10321–10324, https://doi.org/10.1002/ange.201003917.
[80] A.L. Usler, R.A.De Souza, A critical examination of the Mott–Schottky model of grain-boundary space-charge layers in oxide-ion conductors, J. Electrochem. Soc. 168 (2021), 056504, https://doi.org/10.1149/1945-7111/abfb37.
[81] D.S. Mebane, R.A.De Souza, A generalised space-charge theory for extended defects in oxygen-ion conducting electrolytes: from dilute to concentrated solid solutions, Energy Environ. Sci. 8 (2015) 2935–2940, https://doi.org/10.1039/C5EE02060C.
[82] W. Rheinheimer, J.P. Parras, J. Preusker, R.A. De Souza, M.J. Hoffmann, Grain growth in strontium titanate in electric fields: The impact of space-charge on the grain-boundary mobility, J. Am. Ceram. Soc. 102 (2019) 3779–3790, https://doi.org/10.1111/jace.16217.
[83] R.A. De Souza, E.C. Dickey, The effect of space-charge formation on the grain-boundary energy of an ionic solid, Philos. Trans. R. Soc. A. 377 (2019) 20180430, https://doi.org/10.1098/rsta.2018.0430.